A hydromechanical biomimetic cochlea: Experiments and models

Fangyi Chen[a)]
Department of Electrical and Computer Engineering, Hearing Research Center, Boston University, Boston, Massachusetts 02215

Howard I. Cohen
Department of Physiology and Biophysics, Boston University, School of Medicine, Boston, Massachusetts 02118

Thomas G. Bifano
Department of Manufacturing Engineering, Boston University, Boston, Massachusetts 02215

Jason Castle, Jeffrey Fortin, and Christopher Kapusta
General Electric Global Research Center, Niskayuna, New York 12309

David C. Mountain and Aleks Zosuls
Department of Biomedical Engineering, Hearing Research Center, Boston University, Boston, Massachusetts 02215

Allyn E. Hubbard[b)]
Department of Electrical and Computer Engineering, Department of Biomedical Engineering, Hearing Research Center, Boston University, Boston, Massachusetts 02215

(Received 11 May 2005; revised 1 November 2005; accepted 3 November 2005)

The construction, measurement, and modeling of an artificial cochlea (ACochlea) are presented in this paper. An artificial basilar membrane (ABM) was made by depositing discrete Cu beams on a piezomembrane substrate. Rather than two fluid channels, as in the mammalian cochlea, a single fluid channel was implemented on one side of the ABM, facilitating the use of a laser to detect the ABM vibration on the other side. Measurements were performed on both the ABM and the ACochlea. The measurement results on the ABM show that the longitudinal coupling on the ABM is very strong. Reduced longitudinal coupling was achieved by cutting the membrane between adjacent beams using a laser. The measured results from the ACochlea with a laser-cut ABM demonstrate cochlear-like features, including traveling waves, sharp high-frequency rolloffs, and place-specific frequency selectivity. Companion computational models of the mechanical devices were formulated and implemented using a circuit simulator. Experimental data were compared with simulation results. The simulation results from the computational models of the ABM and the ACochlea are similar to their experimental counterparts. © *2006 Acoustical Society of America.* [DOI: 10.1121/1.2141296]

PACS number(s): 43.64.Bt, 43.64.Kc, 43.60.Qv [BLM] Pages: 394–405

I. INTRODUCTION

The cochlea, which is highly frequency selective, handles acoustic phenomena hydromechanically, resulting in an audible frequency range of typically 20 Hz to 20 kHz for humans. Although the biological cochlea is an active mechanism, in which amplification takes place (Dallos, 1996), the passive (aged or slightly damaged) cochlea is still a valuable hearing asset. A passive artificial hydromechanical implementation of a cochlea, therefore, should be able to mimic at least some useful aspects of cochlear signal processing functionality. Modern micromachining technology offers the technology with which to build such a device. In this paper, we describe the construction and characterization of a hydromechanical artificial cochlea (ACochlea). Our goal in this paper is twofold. One is to demonstrate cochlea-like features in the experimental results taken from a prototype device. The other is to use mathematical models[1] to understand the behavior of the prototype and investigate ways to improve its performance.

To mimic salient cochlear signal processing features, electronic chips have been built using both analog (for a review see Yang, 2004) and digital circuits (for a review see Leong *et al.*, 2003). Most of the analog implementations are improved versions of the electronic cochlea originally proposed by Lyon and Mead (1988). In these implementations, a cascade of second-order filters was built using subthreshold

[a)]Current address: Oregon Hearing Research Center, Oregon Health & Science University, Portland, Oregon 97239-3098. Electronic mail: chenfa@ohsu.edu
[b)]Author to whom correspondence should be addressed: Allyn E. Hubbard, Boston University, Department of Electrical and Computer Engineering, 8 Saint Mary's Street, Boston, Massachusetts 02215. Electronic mail: aeh@bu.edua

MOSFET technology. This implementation, however, suffers stability and accuracy problems from transistor mismatching and temperature sensitivity.

The digital implementations to approximate the cochlear frequency response are built as digital filters, either coded into a field programmable gate array (FPGA), designed into an application-specific integrated circuit (ASIC), or programmed on a digital signal processing (DSP) chip. The digital implementation typically requires more transistors than a comparable analog implementation, so the number of output channels from a single digital chip is likely to be more limited. Another problem is that, while a larger number of output channels can be achieved with increasingly potent chips, or by using multiple chips, the power consumption can become unattractively high.

A mechanical implementation of an artificial cochlea should be able to mimic cochlear signal processing functionality in a more natural way. The desired behavior should be the result of material properties and construction geometry, not circuit behavior. In theory, the mechanical signal processor does not require external power other than the acoustic power from the impinging sound, although electrical power will be needed for instrumentation and post-processing.

The history of building a mechanical structure for simulating cochlear behavior can be divided into two periods. During the first period, mechanical cochleae were built to study and help understand cochlear behavior. Because of the difficulties building and driving such a small device, these early mechanical cochleae were typically one or two orders of magnitude larger than a human cochlea. A *scaling* technique was adopted in those designs, wherein all the dimensions of the human cochlea were multiplied by a scale factor. However, the material properties of these artificial cochleae were usually not scaled properly due to the lack of materials with the required properties. Some of the important works of this period are as follows. von Bekesy (1960) built a mechanical cochlea to study the traveling wave. Tonndorf (1959) adopted a similar structure to study beats in the cochlea. Chadwick and Adler (1975) constructed a mechanical cochlear model to examine their theory of the cochlea. Much later, Lechner (1993) implemented an ACochlea with a Polyvinylidene Fluoride (PVF_2 or PVDF) bending transducer, which is mounted on beams on the artificial basilar membrane (ABM) to obtain an electrical output from the vibrational activity. Lechner also added actuators to a beam to simulate the active response in the cochlea. About the same time, Zhou *et al.* (1993), proposed the first life-sized physical mechanical cochlea. In this device, an isotropic polymer membrane was put on a steel template to build the ABM. Two plastic chambers were constructed to mimic the cochlear scalae.

The second period begins in the mid-1990s. With improved micromachining technology, efforts to build practical devices to mimic the cochlear function were carried out and reported. Haronian and Macdonald (1996) proposed a microelectromechanically based frequency signature sensor (MEM-FSS). An array of beams of gradually varying lengths was etched on a silicon substrate. However, no fluid coupling exists in this structure. Thus, the structure can only mimic the basilar membrane (BM), since the fluid coupling is a key element for the cochlea mechanical signal processing. Although they did model the squeezed air between beams as a coupling spring and dashpot, they treated this coupling as a local factor to influence the adjacent beam resonating quality, but not a longitudinal energy coupling mechanism. Tanaka *et al.* (1998) described a fish-boned structure, where different lengths of silicon beams lie on a core backbone of the same material. This core backbone was used to transfer vibrations along the device, simulating the fluid channel's function. The input to the device is at the end of the core backbone, which is too stiff to match it properly to the acoustic input signal. Lim *et al.* (2000) published their work on a mechanical cochlea made by laying an isotropic film over a slotted silicon wafer and surrounding it with fluid channels. They demonstrated the traveling-wave feature by showing the phase plot at two locations along their ACochlea. The magnitude response shown is rather irregular and does not show the expected high-frequency roll off. The author offered the isotropy of the ABM as the major reason for this problem. Hemmert *et al.* (2003) proposed a fluid-filled MEMS-based mechanical cochlea. In this model, the BM is built using an epoxy-based photoresist, which possesses stiffness close to the biological material. The authors used the impulse response at two very closely spaced locations to demonstrate the existence of a traveling wave.

Recently, Wittbrodt *et al.* (2004) proposed a new design continuing Lim's effort (Lim *et al.*, 2000). Aluminum fibers were deposited on a soft membrane to produce the anisotropic ABM. In 2002, White and Grosh (2002) reported their microelectromechanical-system (MEMS) cochlea, which used a single fluid channel and a BM made of silicon beams. Silicon-nitride beams were used in a newer version of this work to reduce the residue tension on the beams (White and Grosh, 2005). Both the silicon and silicon-nitride beams are much stiffer than their biological counterpart. White and Grosh (2005) presented the measurement results from their ACochlea. The phase response from measurements on this device demonstrated the traveling wave delay. However, the magnitude response shows very shallow high-frequency rolloff with ripples. The authors cited the difficulty in achieving strong enough anisotropy on the ABM as a reason for the shallow high-frequency rolloff. To obtain an electrical output from the beam vibration, White and Grosh (2002) used piezoresistive material and later (White and Grosh, 2005) used a capacitive sensing technique.

The above review demonstrates some of the challenges in building an ACochlea. The first challenge is the fabrication. Here the key is to build an anisotropic BM with stiffness similar to the biological material. The second challenge is to properly drive the small device and demonstrate the cochlea-like features in the experimental results. Those features include a slow traveling wave, sharp rolloff at the high-frequency end of the beam vibration spectrum, and the gradually decreasing cutoff frequency of the beam vibration spectrum along the length of the ACochlea.

The passive hydromechanical cochlea is typically simplified to be an elongated box with two fluid channels and a membrane partition between them (Peterson and Bogert,

1950; Zwislocki, 1950). The membrane partition is sometimes simply called the "basilar membrane". It is the BM, in fact, whose stiffness is critical to cochlear frequency sensitivity (von Bekesy, 1960). Zwislocki (1950) proposed a transmission-line-based model for his simplified cochlear mechanical structure. His theory explained the presence of a traveling wave as well as the tonotopicity of the cochlea. These two important features of cochlear behavior were originally measured by von Bekesy (1960). Zwislocki (1950) noted that the stiffness gradient on the BM, and the presence of the fluid channel, are keys to the hydromechanical signal processing in the cochlea. The interaction of the fluid mass and the BM stiffness results in the passive cochlear response, which present a series of low-pass filters with gradually varying cutoff frequencies.

Two devices are described in this paper: One is an ABM and the other is an ACochlea built around the ABM. The ABM is the most important functional part of the ACochlea, since it provides tonotopicity, i.e., positional frequency selectivity. We also provide computational models of the devices. Results from those devices are presented to characterize their performance and to help us to understand their behavior. The measured results on our ACochlea demonstrate some cochlea-like features, such as the slow traveling wave, tonotopicity, and the sharp high frequency roll-off. The model results mimic the performance of the devices.

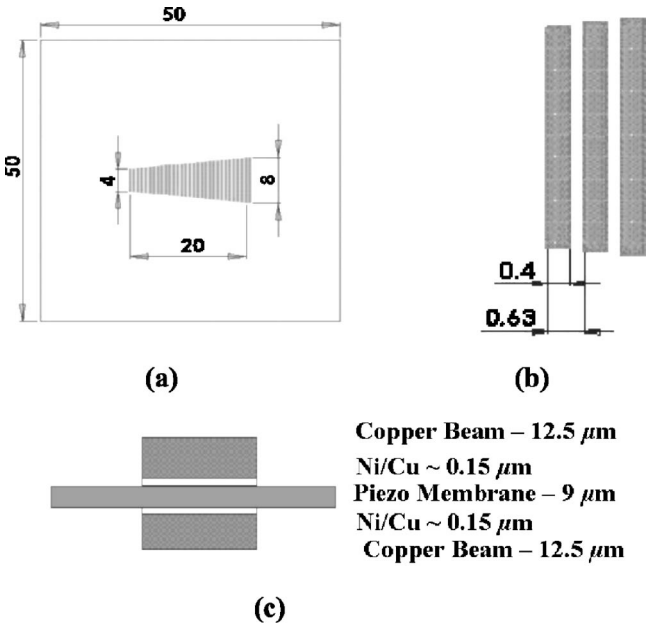

FIG. 1. The membrane structure of a 32-beam ABM, not to scale. The dimensions in this figure are in mm unless specified otherwise. (a) The layout schematic. This panel shows how the beams are arrayed on the membrane substrate. (b) Zoom-in view of the beam structure. (c) A schematic of the cross-sectional view of a beam section.

II. METHODS

A. Device design and fabrication

We constructed our ACochlea with our ABM and a fluid channel. The constituents of the ABM include a membrane substrate with beams and the frame supporting it. On the membrane substrate, a Cu beam array with gradually increasing length is designed to produce the stiffness gradient, which is a key component for the cochlear mechanical signal processing. The beam array has a trapezoidal profile. Frames support the membrane. The frames have a slotted window of the same shape as the profile of the Cu beam array. When the membrane is sandwiched by the frame, the edge of the slotted window clamps the beams and forms an open channel on each side of the membrane. This open channel is covered by a Plexiglas structure to form the ACochlear fluid channel. Two windows on this Plexiglas structure provide accessibility to the fluid channel, one for providing mechanical input and the other for fluid filling.

1. ABM materials and structure

The fabrication and assembling of the ABM took place in General Electric's Global Research Center (GE-GRC) facility in Niskayuna, NY. The membrane substrate is made of piezofilm procured from Measurement Specialties, Inc. of Hampton, VA. The piezo film at the beam serves as a mechanical transducer. The current design uses a 9 μm thick PVDF film premetalized with ~1500 angstroms Ni/Cu on both sides.

During the fabrication, a 100 mm diameter sheet of the piezofilm was first attached to a hoop around the outside, using a laminating process. This process induces a slight pretension in the film, which achieves a smooth surface so that standard photolithography can be used to form the beam array and the circuitry to connect the piezosensors. The smooth surface is also needed in assembling the ABM.

AZ1512, a positive photoresist, is then spun onto both sides of the stretched film. Next, vias are drilled through the stretched frame using the ESI laser system. These vias will be used later for precision alignment pins and alignment locations for the circuitry. Using a laser exposure system, the outline of the circuitry is patterned into the resist on both sides of the frame. AZ351, an aqueous developer (Clariant Corporation, Somerville, NJ) is used to develop the resist and to expose the metal circuitry for electroplating. The developing time is about 3–5 min. If interconnections between both sides of the film are necessary, the ESI laser system can be used to drill through the material to form fused vias.

Since the metallization of the PVDF film is very thin, the circuitry is electroplated with Cu to about 12.5 μm thick. This gives the device rigidity for probing and the correct beam modulus. Following plate-up, the resist is stripped from both sides and then redeposited for the next patterning step. After developing, the device is wet etched in a 30% nitric acid bath to remove the Ni/Cu metallization. Etching takes about 1 min, depending on the concentration of the solution. This in turn exposes the PVDF film and defines the circuitry. Once etching is complete the remaining resist can be stripped to expose the completed circuit.

Figure 1(a) is a schematic view of the membrane substrate, showing a beam array in the middle. The circuitry to connect beams is not shown here for simplicity. The beam length increases progressively from 4 mm at one end to 8 mm at the other end. This length gradient produces the stiffness gradient. There are 32 beams on this sample. Figure

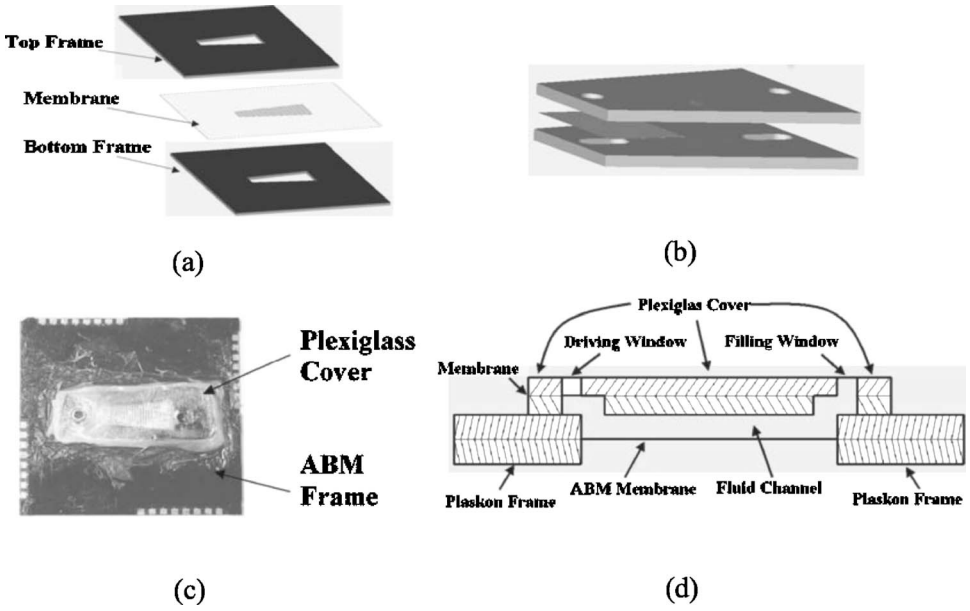

FIG. 2. The constituents of the ACochlea. (a) The ABM. The membrane substrate of the ABM is sandwiched by two Plaskon (a plastic material) frames. Each frame has a trapezoidal slot of the same size as the profile of the beam array. (b) The Plexiglas cover. The cover encloses the trapezoidal slot on the frame of the ABM, forming the ACochlear fluid channel. (c) Photo of the assembled ACochlea. The ACochlea is made by gluing the Plexiglas cover onto the frame of the ABM. The four-row connectors at the edge of the frame are to obtain electrical output from the piezoelectric beams. (d) Schematic of a cross-section view of the ACochlea. This panel demonstrates the relationship between the Plexiglas cover, the ABM, and how the canals on the bottom piece of the cover connect the windows to the ACochlear fluid channel.

1(b) shows a zoom-in view of the beams. On the sample under discussion, the beams are equally spaced along the ABM, each being 400 μm wide. They are spaced 630 μm center to center, resulting in a gap of 230 μm between the edges of adjacent beams. Figure 1(c) shows a schematic cross-sectional view of a beam section, noting the thickness dimensions of the layers. This figure shows that the two Cu layers, each of 12.5 μm thickness, are coated on both sides of the piezomembrane.

The Young's modulus of the Cu is about 30–50 times greater than that of the piezomembrane (110 GPa vs. 2–4 GPa). Hence this structure is expected to produce strong anisotropy. However, a later study showed that the pretension on the membrane during the fabrication greatly reduces the anisotropy. Therefore, a laser system (model #5200 from ESI in Portland, OR) was used to provide controlled, sharp, precision cutting or slitting of the film. The spot size of this triple YAG laser is about 18 μm. The laser slices through the membrane, resulting in a cut of about 100 μm width in the membrane between beams.

The frame of the ABM is made of plaskon (Amco Plastic Materials, Inc. in Farmingdale, NY), a thermo set epoxy widely used in the electronics industry as an encapsulant. It was chosen because of its ease of fabrication. The plaskon is molded into a large substrate, 6 in. by 6 in., and approximately 1 mm thick. The thickness will dictate the depth of the ACochlear fluid channel, as we will discuss in Sec. II A 2. If a different substrate thickness is needed, the plaskon can be lapped thinner or molded to the desired thickness. Post-molding, the plaskon is cleaned with an acetone wipe followed by a propanol wipe. This allows better adhesion to the adhesive layer. The adhesive layer is a 3M™ high-temperature acrylic film, similar to a double-sided tape. The adhesive is applied to the appropriate sides of the plaskon and trimmed with a razor blade. The adhesion process is used to sandwich the membrane substrate in the assembly of the ABM.

2. Assembly of the ABM

Figure 2(a) shows how two identical Plaskon frames are used to support the membrane substrate. The frames were cut by the laser into the same shape as the membrane substrate. A trapezoidal window, which is of the same size as the profile of the Cu beam array on the membrane substrate, was opened on the frames.

A laminating process is used to create this sandwich. The plaskon pieces are attached to the prestretched membrane by removing the release sheet from the 3M™ adhesive and adhering the plaskon part to the PVDF film. Precise alignment with pins permits the two long edges of the trapezoidal windows to firmly clamp the far tip edges of the Cu beams. In this way, the frames support the membrane substrate, while the window exposes the beam array. Because of the frame thickness, typically 1 mm on both sides of the beam array, we create the fluid channel by covering one open channel using the Plexiglas cover and filling it with water. The fluid channel is 4 and 8 mm wide at the small and large end, 20 mm long, and 1 mm high. The fluid channel provides longitudinal energy coupling.

3. Assembly of the Plexiglas cover

Figure 2(b) illustrates the assembly of the Plexiglas cover and how it forms a closed fluid channel. This cover is about 35 mm long, 10 mm and 15 mm wide at the small and large ends, respectively. Windows are opened on each end. A 2 mm window accommodates the piezostack driver to stimulate the ACochlea. The channel is filled through the other window and sealed with Vaseline.

On the bottom of the Plexiglas piece [Fig. 2(b)], two channels, each of about 3 mm long and 2 mm wide, are opened to provide a connection between the windows and the ACochlear fluid channel. Between the top and bottom pieces, a soft membrane is placed underneath the driving window. This membrane is sandwiched by the top and bottom Plexiglas pieces by applying Krazy Glue®. The mem-

brane window separates the ACochlear fluid channel from the air and provides an interface for the piezodriver.

4. Constituents of the ACochlea and the method to fill the fluid channel

Figure 2(c) shows the assembled ACochlea. The Plexiglas cover is adhered to the Plaskon surface over the ABM using a commercially available, quick setting, epoxy adhesive (Plastic Welder™ from Devcon). Figure 2(d) shows a schematic of the cross-section view along the longitudinal axis. This view shows that the driving and filling window are connected to the ACochlear fluid channel through the two canals on the bottom piece of the Plexiglas cover. To fill the fluid channel, the whole ACochlea, as shown in Fig. 2(c), is placed in a vessel and submerged in water and degassed using a vacuum.

5. Efficacy of the design of our ACochlea

Our device is designed to mimic the passive cochlear mechanical signal processing features of the cochlea, not its size, shape, or material properties. Only the top open channel of the ABM is covered. The bottom of the ABM is exposed to the air, so that our laser instrument could monitor the beam's vibrational activity. When a double channel implementation was used, where both channels were covered by a Plexiglas piece, the plastic cover, and the fluid absorbed, deflected and scattered the laser light, both during incidence and reflection, degrading the signal-to-noise ratio of the measurement. Theoretical analyses (Patuzzi, 1996) and the modeling study by an author (Chen, 2005) show that the single channel cochlea offers behavior very similar to its double channel counterpart.

B. Experimental measurements

We measure both the ACochlea and ABM responses by recording the vibration of the beams along the ABM. However, because of the different structure of the ACochlea and ABM, very different driving methods were adopted. Figure 3 shows a block diagram of the experimental setup for testing the acoustic properties of the ABM.

1. Schematic of the test system and the procedures for ABM measurements

In the setup shown in Fig. 3, a pulse signal is generated from an HP8114A Pulse Generator to drive the speaker with a 6 V, 32 μs, 10 per second signal. The interval of almost 100 ms allows sufficient time for the acoustic signal to die out. The speaker generates a peak sound pressure of about 1.0 Pa peak amplitude having approximately a 30 kHz bandwidth. A Brüel and Kjaer Condenser Microphone Type 4138 placed 2–3 mm from the beams measures the sound pressure near the beams. Simultaneously, the beam vibration is observed and measured by a Laser Doppler Vibrometer (LDV) system from Polytec PI, Auburn, MA. The laser head of the LDV system is 750 mm from the ABM, on the other side from the microphone. Both the amplified microphone signal and LDV output signal are sampled by a Tektronix digital oscilloscope model TDS420A.

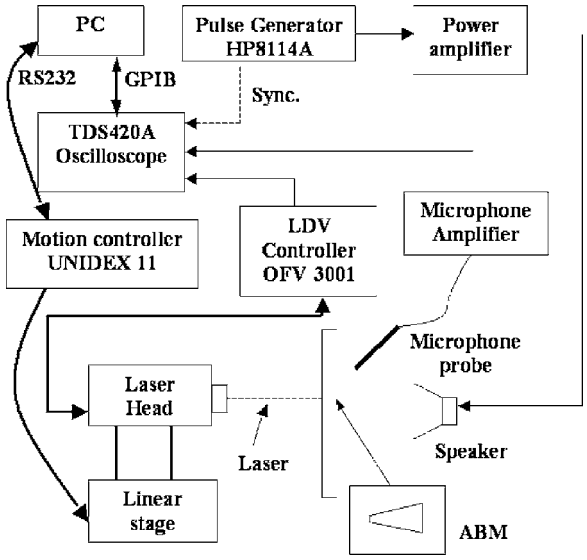

FIG. 3. Experimental setup for the ABM measurement. The pulse generator HP8114A generates a stimulus to drive the speaker through a power amplifier. The resulting sound pressure, which is measured by a B & K 1/8th in. microphone, makes the beams on the ABM vibrate. This vibration is detected by the laser from the laser head OFV303. The detected vibration signal is then decoded in the LDV controller OFV3001. The decoded vibration signal and the sound pressure signal were sampled by a digital oscilloscope TDS420A. A PC reads data from the oscilloscope through a General Purpose Interface Bus (GPIB). To measure the vibration at different locations along the ABM, the laser head is placed on a motorized linear stage ATS302. The linear stage is controlled by a remote controller Unidex 11, which has a keyboard to manually manipulate the motion of the stage. The controller also has an RS-232 interface with the PC, which allows for the automatic control.

The samplings are triggered by a synchronizing signal from the pulse generator. The measurement is averaged over approximately 100 repetitions. Using the GPIB protocol a PC reads the sampled data from the TDS420A. A Fast Fourier Transform (FFT) is used to calculate the sound pressure spectrum and the beam velocity spectrum from the time domain data. The beam sensitivity spectrum is calculated by dividing the beam velocity spectrum by the sound pressure spectrum. The impulse response of the beam sensitivity is calculated by doing an inverse FFT (IFFT) on the resulting sensitivity spectrum. The laser head of the LDV system is placed on a linear translation stage, an ATS302, manufactured by Aerotech Inc. of Pittsburg, PA. It is controlled by another Aerotech product, a motion controller, the Unidex 11. Computer interfacing is done through an RS-232 connection. Through the controller, the stage and the laser can be moved laterally with an accuracy of 2 μm over in a range of 50 mm.

2. Single beam measurement

Modal frequencies of the beam vibration were examined to investigate if the tension force on the beam is significant. Haronian (Haronian and MacDonald, 1996) and White (White and Grosh, 2002) also explored tensioning on the beams of their ABMs, by checking the relationship between modal frequencies. The measurement procedure is the same

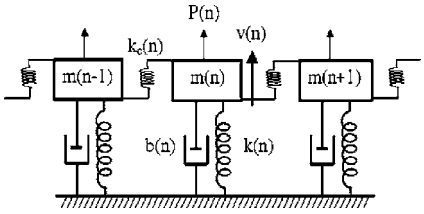

FIG. 4. The mechanical model of the ABM. In this model, each beam is modeled as a mechanical resonator with a mass component, $m(n)$, a damper, $b(n)$, and a spring, $k(n)$. The spring, $k_c(n)$, connecting two beam resonators, represents the coupling between beams through the membrane substrate.

as that used for the ABM measurement, except that the ABM is mounted so that the beam is in the horizontal direction and the laser scans along the length of the beam.

3. ACochlea measurement

The basic experimental setup shown in Fig. 3 is also used to measure the ACochlear response, but using a piezostack driver. The driver head, a cylindrical steel post of 10 mm length and 2 mm in diameter, was glued on top of the stack driver. The piezostack was then glued on an aluminum post, which was mounted on an XYZ micromanipulator to move the driver head into the driving window. The piezostack driver's vibration was measured before it was advanced into the driving window. The load of the ACochlea should not influence the vibration of the driver, because the acoustic impedance of the driver is at least 100 times larger than that of the ACochlea, as calculated using our mathematical models. Their outputs track the ACochlear and piezodriver response well.

We also tested an ACochlea built using an ABM where the piezofilm between beams was sliced completely through, to reduce longitudinal coupling. The cuts allow slow water leakage from the ACochlear fluid channel. Measurements typically had to be done within 30-45 min, before significant leakage would occur.

C. Simulation methods

1. Mechanical model of the ABM

Here the ABM model is introduced using its mechanical schematic. Each metal beam is represented by a damped mass-spring oscillator. Contrary to the classical cochlear model (von Bekesy, 1960), where the coupling between the BM sections is ignored, most models of artificial cochlea include longitudinal coupling. Lim (Lim *et al.*, 2000) indicated that the longitudinal coupling can influence the slope of the high-frequency rolloff of the artificial cochlea responses. White and Grosh (White and Grosh, 2005) also use the longitudinal stiffness to account for the shallow rolloff in their measurements. Here a spring is used to represent the coupling action of the membrane between the beams. Figure 4 shows the mechanical schematic of three adjacent beams.

2. Circuit model of the ACochlea

Figure 5 shows a circuit model of the ACochlea, which is a two-dimensional version of a traditional transmission-line structure (Peterson and Bogert, 1950; Zwislocki, 1950);

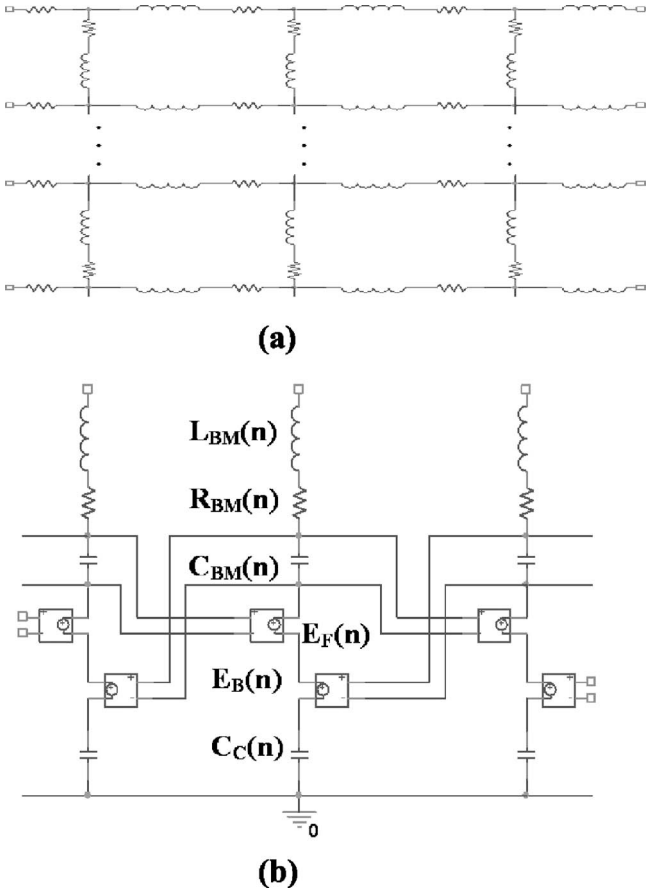

FIG. 5. The circuit schematic for three adjacent beam sections of the ACochlear model. (a) The fluid channel model. The inductors and resistors here represent the fluid inertia and viscosity, respectively. (b) The ABM model. This is the circuit (acoustic units) implementation of the mechanical model shown in Fig. 4. The dashpot damper $b(n)$, spring $k(n)$, and mass $m(n)$ are replaced by resistance $R_{\mathrm{BM}}(n)$, capacitance $C_{\mathrm{BM}}(n)$, and inductance $L_{\mathrm{BM}}(n)$, respectively. The values of the circuit components for a beam section are determined by the beam geometry and its material characteristics. The effect of the interstage spring $k_c(n)$ between beams is represented by two voltage controlled voltage sources (VCVSs), $E_F(n)$ and $E_B(n)$, and the capacitor $C_C(n)$. This seemingly complex circuit is necessary to match the force equation of the mechanical coupling. The value of the coupling components is determined by the geometry of the membrane and the pretension on the membrane. The floating nodes at the bottom of the fluid model are connected to those on the top of the ABM model, forming the ACochlear model.

(see Hubbard and Mountain, 1996) for a review. Figure 5(a) shows the fluid channel, modeled as a two-dimensional matrix of inductors and resistors, representing the inertia and the viscosity of the fluid, respectively. Figure 5(b) shows a circuit model for the ABM, which represents the mechanical model shown in Fig. 4, now based on the electroacoustic analogy. Each beam is modeled as a series of circuit components, and is called a beam section. A middle section receives input both from the one before it and the one after it, affecting the longitudinal coupling. The fluid channel model is constructed with an equal number of sections and connected one-to-one with the ABM model, forming the ACochlea model. Table I lists the corresponding components in the acoustical model and the circuit model, as well as their dimensional units.

The stiffness of the beam section is due to the bending and the pretension on the beam, and labeled T_y to distinguish

TABLE I. Corresponding components in the acoustical model and the circuit model, as well as their dimensional units. Note that the components in the mechanical model are in acoustic units. k_C is the coupling spring that represents the longitudinal coupling, which is represented in the circuit model by two VCVSs and a coupling capacitor. Although the unit of the VCVS is Pa, the gain of VCVSs is dimensionless.

Acoustic	Circuit	Unit
P: pressure	v: voltage	Pa
V: volume velocity	i: current	M^3/s
m: mass	L_{BM}: inductor	kg/m^4
k: spring	$1/C_{BM}$: capacitor	$kg/(m^4\ s^2)$
b: damper	R_{BM}: resistor	$kg/(m^4\ s)$
k_C: coupling spring	E_B: VCVS	Pa
	E_F: VCVS	Pa
	$1/C_C$: capacitor	$kg/(m^4\ s^2)$

it from the longitudinal tension (T_x) on the membrane. The stiffness due to bending is calculated by assuming a clamped–clamped boundary condition on the sandwich structure shown in Fig. 1(c). The stiffness due to the pretension T_y is calculated from a string equation. The value of T_y is estimated in the single beam measurement by observing how the modal frequencies of a beam section deviate from those of an ideal clamped–clamped beam.

In each beam section, the value of the capacitor $C(n)$, which is a volume compliance, is calculated using the square of the beam surface area divided by the total stiffness. The value of inductor $L(n)$ is calculated from the beam acoustic mass, which is the mass of the beam scaled by the square of the beam surface area. The value of the damper, $R(n)$, is calculated from $L(n)$ and $C(n)$ by assigning a quality factor, Q.

The membrane between beams is modeled as a string with tension, represented by the coupling spring $Kc(n)$. By assigning a pretension T_x, the coupling spring value is calculated by knowing the length and the cross-section area of the membrane. Three coupling components $E_F(n)$, $E_B(n)$, and $C_C(n)$ are used to represent the coupling spring in order to satisfy the mechanical equations. The values of Q and T_x are estimated in the ABM study by matching the measured results with modeling results of a proper Q and T_x. [See Chen (2005) for details.]

III. EXPERIMENTAL RESULTS

A. The ABM

1. Results from an ABM with membrane coupling between beams

We measured beam vibration at the middle of each beam on a 64-beam ABM. Figures 6(a) and 6(c) show the spectra of the ABM response. Figure 6(a) shows the spectrum of Beam #32 and Fig. 6(c) shows a gray-scale map of the spectra of all the beams, from Beam #1 at the small, narrower end to Beam #64 at the large, wider end. Figure 6(a) is a cross-section view of Fig. 6(c) at Beam #32. Although Fig. 6(a) exhibits a seemingly irregular spectrum, by looking at the gray-scale map in Fig. 6(c), one can see that there is a pattern in how the spectrum of each beam relates to the others.

Figures 6(b) and 6(d) show the impulse response of the ABM. Figure 6(b) is the impulse response of Beam #32. The figure shows two distinct times when the beam oscillation is strong. The first oscillation lasts from 0.0 to 0.5 ms; the second one starts aggressively at about 1.3 ms and gradually decays in amplitude. A third region of oscillation appears at around 2.8–3.3 ms.

Figure 6(d) shows two distinct triangular-shaped regions, as annotated by the dashed lines. The first is shaped like a right triangle and is positioned at the leftmost side of the 3-D map; the second one is in the middle of the map and has an isosceles triangular shape, although its right-hand edge is not very clear. Figure 6(b) is a cross-sectional line graph through Fig. 6(d) at Beam #32.

2. Results from an ABM with cuts in the membrane between beams

To confirm that the longitudinal coupling on the membrane between beams results in the high-frequency ripples in the ABM spectra, the membrane between beams on a 32-beam ABM was cut using the laser. Figure 7(a) shows the spectrum of Beam #16 and Fig. 7(b) shows a gray-scale spectrum map of all 32 beams. In Fig. 7(a), a clear resonance peak occurs at about 2.8 kHz. The second peak that is the third mode of beam vibration occurs at about 10 kHz. The second mode is not observed because we measured in the middle of the beam, where the second mode has a node; and because the beam is driven by a uniformly distributed pressure (Chen, 2005). This symmetric force tends to suppress the even modes. This is shown in Fig. 8 and discussed later.

B. Single beam

Figure 8(a) shows the vibration spectra of a beam from the 32-beam ABM, with cuts through the membrane, measured at the quarter-length point along the beam. This point is chosen to best observe the second mode. Figure 8(b) shows the 3-D spectral map of the all beam's vibration characteristics.

C. ACochlea

The measured results on an ACochlea, made using an ABM with cuts between beams, are presented in Fig. 9. Figure 9(a) shows the time domain displacement response of Beams #6, 16, and 26. Figures 9(b) and 9(c) show, respectively, the magnitude and phase of the ratio of the beam displacement spectrum to the driver displacement spectrum. (The driver displacement spectrum of the piezostack driver was measured before it was advanced into the driving window).

D. The piezomembrane output

The piezomembrane voltage output from a beam on an ACochlea was measured using the impulse stimulation. We recorded both the displacement of the membrane and the piezoelectrical output of the beam. Figures 10(a) and 10(b) show the time domain response of the displacement and the electrical output from a beam. The electrical output of the

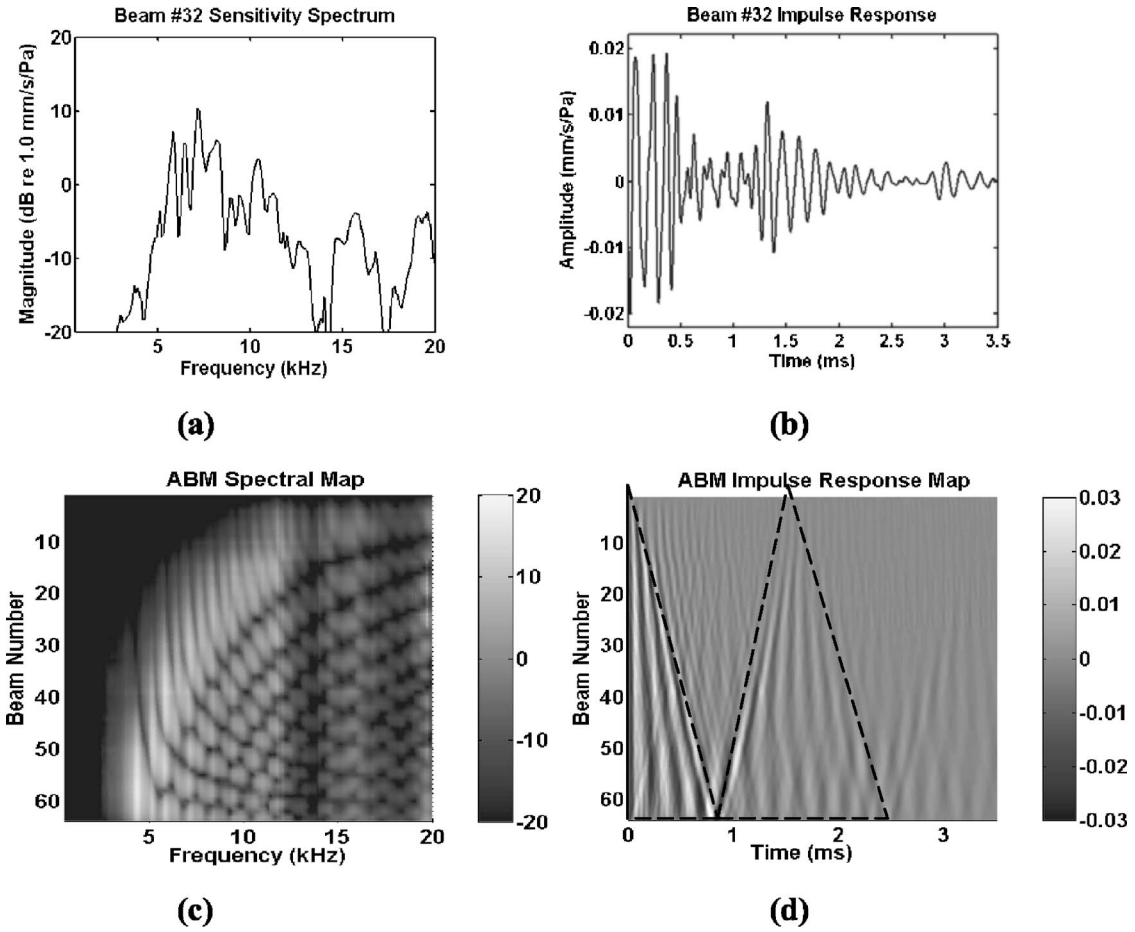

FIG. 6. The velocity sensitivity spectra and the impulse response of a single beam (#32) as well as that of all 64 beams. (a) Magnitude response of the velocity sensitivity spectrum of Beam #32. This spectrum was calculated by scaling the Beam #32 velocity spectrum by the sound pressure spectrum, which was previously smoothed using a median filter to avoid introducing noise. In the test, time domain responses of the sound pressure and the beam response were recorded and their spectra were calculated by taking the FFT of the time domain response. (b) Impulse response of Beam #32. This impulse response is calculated by doing an inverse FFT of the complex spectrum, whose magnitude is shown in (a). (c) A 3-D map of the sensitivity spectrum of all 64 beams. The *X* axis is the frequency and the *Y* axis is the beam number. The magnitude of the velocity of a specific beam at a specific frequency is represented by the gray scale at the corresponding position in the map. Light is highest, dark is lowest. In the *Y* axis, Beam #1 is at the small end of the ABM and Beam #64 is at the large end. (d) A 3-D map of the impulse response of the 64 beams. The *X* axis here is the time. NOTE: In (a) and (c), to get better resolution, dB is used as the unit, where 0 dB is equivalent to 1.0 mm/s/Pa.

piezomembrane shows a response that is similar to the displacement signal. A spike in the electrical output at about 1 ms is due to electrical coupling directly from the driver signal to the piezo-output to the measurement amplifier. This spike signal was manually removed before calculating the electrical output spectrum. Figure 10(c) shows the sensitivity spectrum of the piezo-output. The sensitivity is about 30 mV/μm at 2 kHz, where the beam vibration is at its maximum.

IV. COMPARISIONS OF MODELING AND EXPERIMENTAL RESULTS

A. ABM

The ABM model [Fig. 5(b)] was used to simulate the ABM response. An ac analysis was used to generate the spectral map of the beam responses. An ac voltage source was applied to each beam section, simulating a unit pressure applied to the ABM. The current on each beam section, which represents the volume velocity of the beam, was scaled by the area of the beam to obtain the linear velocity. In Figs. 11(a) and 11(b), the beam response from the simulation, Fig. 11(b), is compared with the calculated beam frequency response from the measured data, Fig. 11(a). Both figures exhibit a wide arching bright band from about 3 to 12 kHz, which is called the major band and represents the beam resonance. Orderly patterned, high-frequency ripples at frequencies above the major band are due to the longitudinal coupling through the membrane between beams.

In the model, the longitudinal tension T_x on the ABM membrane substrate determines the degree of the longitudinal coupling. The modeling study shows that a high T_x on the ABM results in the high-frequency ripples in the frequency map. A smaller T_x will enhance the magnitude of resonant peaks in the major band, with reduction of the response to the right of the major band. Given a relatively limited range of geometries, fluids, and material properties, for which the model is valid, T_x is a critical parameter.

B. ACochlea

Using the ACochlear model shown in Fig. 5, an analysis was performed to calculate the ACochlear model frequency

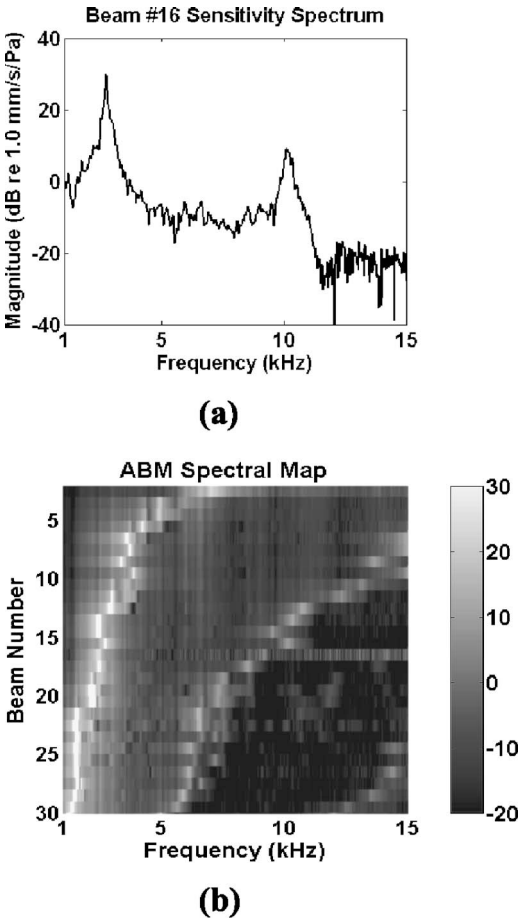

FIG. 7. Measured results on the beams of a 32-beam ABM with cuts through the membrane between beams. (a) The velocity sensitivity spectrum of Beam #16. (b) A three-dimensional map of the beam sensitivity spectrum. The peaks at about 2.8 and 10 kHz in Fig. 7 (a) are the first and third mode of the beam vibration, respectively. Correspondingly, there are two bright bands in the gray-scale map in Fig. 7 (b). A dB scale is used here, and 0 dB corresponds to 1 mm/s/Pa.

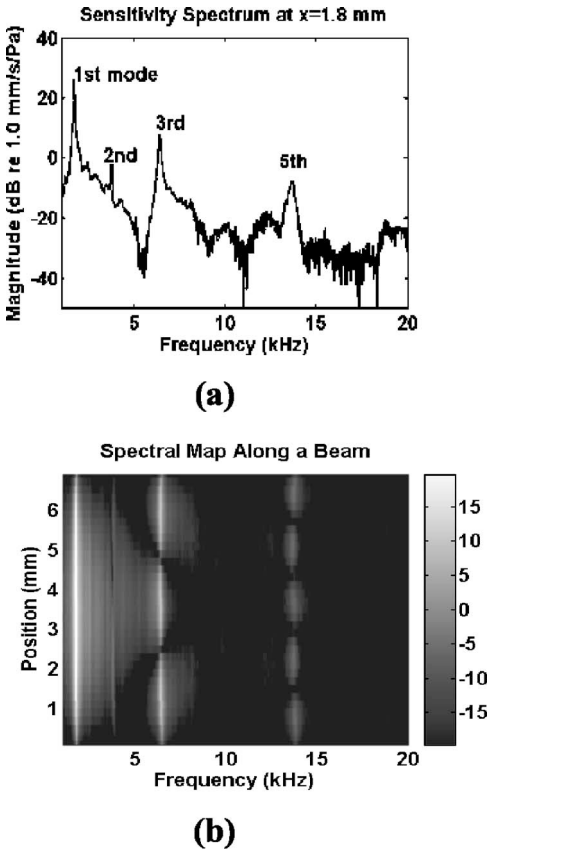

FIG. 8. The velocity sensitivity spectrum of a beam on the 32-beam ABM with cuts through the membrane. (a) Velocity sensitivity spectrum at a location 1.8 mm from the end of the beam. This is about one-quarter the length of the beam. (b) A 3-D spectral map. The *Y* axis marks the positions along the lengthwise direction of the beam. Corresponding to the peaks shown in (a), this map demonstrates the first mode with a long light line at 1.73 kHz, the third mode with three light spots at 6.38 kHz, and the fifth mode with five light spots at 13.7 kHz. The second mode—at 3.79 kHz—can be discerned if one looks for two light, vertical lines at that frequency. The fourth mode is not discernible from Fig. 10(b).

responses to compare with their experimental counterparts. The ratio of the linear velocity of the beam vibration to the piezodriver velocity was calculated to establish the beam transfer response. Figure 12 shows the spectral plots of four equally spaced beams, comparing the measured and modeling results. Figure 12(a) compares the magnitude responses of the four beams; Fig. 12(b) compares their phase responses.

V. DISCUSSION

A. ABM

The results presented in Sec. II A demonstrate the effect of coupling on the membrane substrate of the ABM. First, the spring coupling via the membrane between beams supports a wave propagating along the ABM. In Fig. 6(d), the left edge of the second triangular region changes from 0.9 ms at Beam #64 to about 1.8 ms at Beam #1. This indicates a wave traveling from the large end to the small end, because the wave is a result of the spring coupling due to the membrane substrate rather than due to a mass coupling. Second, the spring coupling also contributes to the rippling appearance of the beam vibration spectra, as shown in Fig. 6(c). The modeling results shown in Fig. 11(b) demonstrate that a larger coupling will produce larger ripples in the spectra. The measurement results in Fig. 7 also support this conclusion by showing that removing the coupling can eliminate the rippling.

In Fig. 7(b), the gray-scale spectral map demonstrates the frequency selectivity of the ABM. The resonant frequency of the beams does not change smoothly with beam number. This is most likely due to a nonmonotonic tension along the beams. As discussed in the single-beam measurement, the tension in the lengthwise direction of the beam contributes to the beam stiffness. The fabrication process, such as Cu deposition and prestretching the membrane during the assembling of ABM, could introduce nonmonotonic tension on beams. The laser cutting may also result in a nonmonotonic change in the pretension on the beam. This change of the pretension will result in a nonmonotonic change in the beam stiffness, and thus affect the expected, monotonic change in resonant frequency of the beam.

B. Single beam

In Sec. II B, we demonstrated the existence of vibrational modes of a single beam. The relationship of the modal

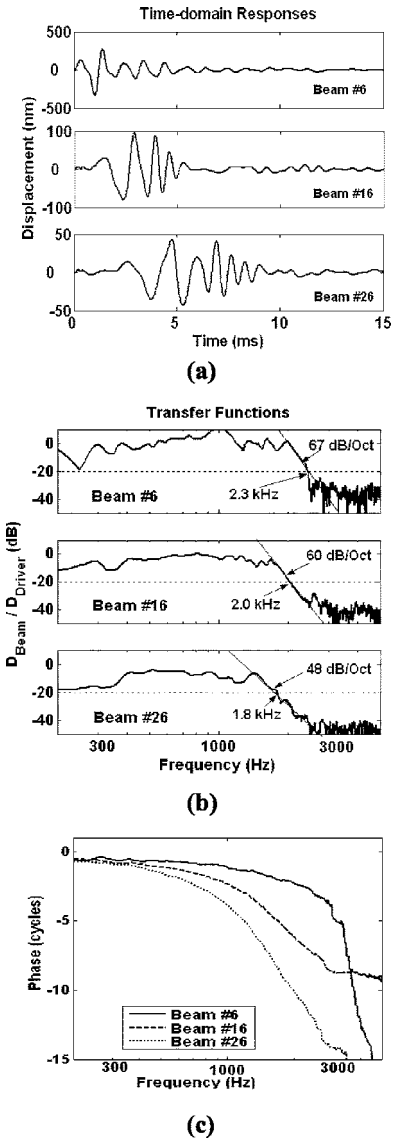

FIG. 9. Displacement measured on beams along the ACochlea made up using the ABM with cuts in the membrane between beams. (a) Time domain response. (b) Transfer function: Magnitude of the ratio of the beam displacement spectrum and the driver displacement spectrum. This high impedance of the driver results in negligible changes on its response after loading with the ACochlea. The frequency where the value of the magnitude response is about −20 dB is defined as the cutoff frequency of that beam. Those frequencies are 2.3, 2.0, and 1.8 kHz for Beams #6, #16, and #26. In the figure, we also marked the slope of the high-frequency rolloff of the response. The response of Beam #16 has a slope of 60 dB/octave. (c) The phase response of the ratio. Phase plots from Beam #6, Beam #16, and Beam #26 show a steady increasing delay until the signal is lost in noise.

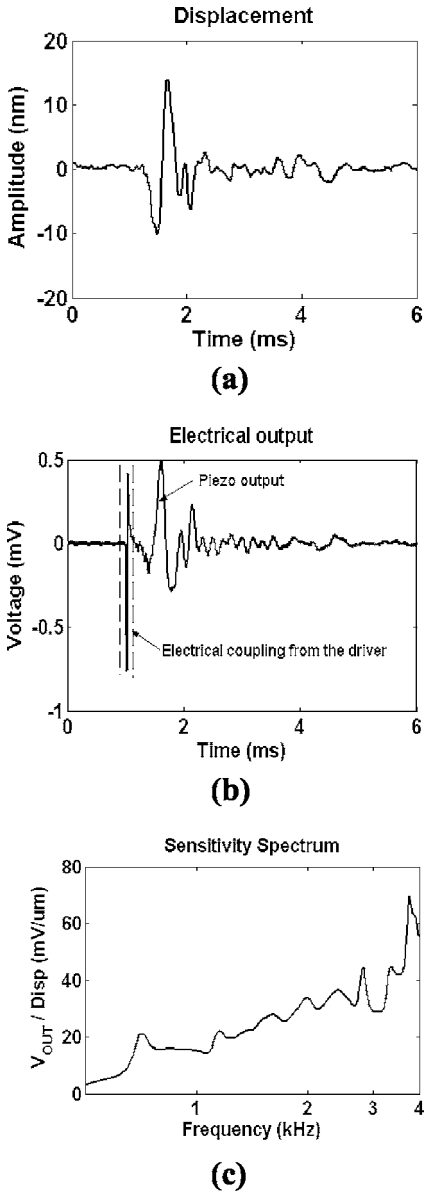

FIG. 10. The impulse response of a beam on an ACochlea. (a) Displacement output. (b) Electrical output. (c) Spectrum of the piezoresponse. This was calculated by scaling the piezoelectric output spectrum by the beam displacement spectrum.

frequencies can be used to ascertain the behavior of the beam (von Bekesy, 1960). Haronian (Haronian and MacDonald, 1996) indicated that the beam in their MEM-FSS behaves like a string instead of an expected clamped–clamped beam. Here we compare the modal frequencies from experimental results with those estimated from the theory for both a string and a pure clamped–clamped beam. For easy comparison, we normalize the higher frequencies using the first mode frequency. From Fig. 8, we note the frequencies of the first, second, third, and fifth modes to be 1.73, 3.79, 6.38, and 13.7 kHz. The normalized frequencies are 1.0, 2.69, 3.69, and 7.92. For a string, the higher mode frequencies are integer multiples of the first mode, so the corresponding normalized frequencies are 1.0, 2.0, 3.0, and 5.0. For a pure clamped–clamped beam, they are 1.0, 2.75, 5.40, and 13.3. Figure 13 plots the normalized frequencies in these three cases. Thus, the beam behavior is somewhere between a string and a clamped–clamped beam. This behavior of the beam is primarily due to the pretension on the beam, T_y.

It is well known that the stiffness of a pure clamped–clamped beam is inversely proportional to the cube of its length. However, the stiffness of a string is inversely proportional only to its length. For the ABM with the same width gradient, a string-like beam array will result in a much smaller stiffness gradient than a pure beam array. The string-like feature of the beam reduces the ABM stiffness gradient, which reduces the frequency range of the ACochlea made using this ABM.

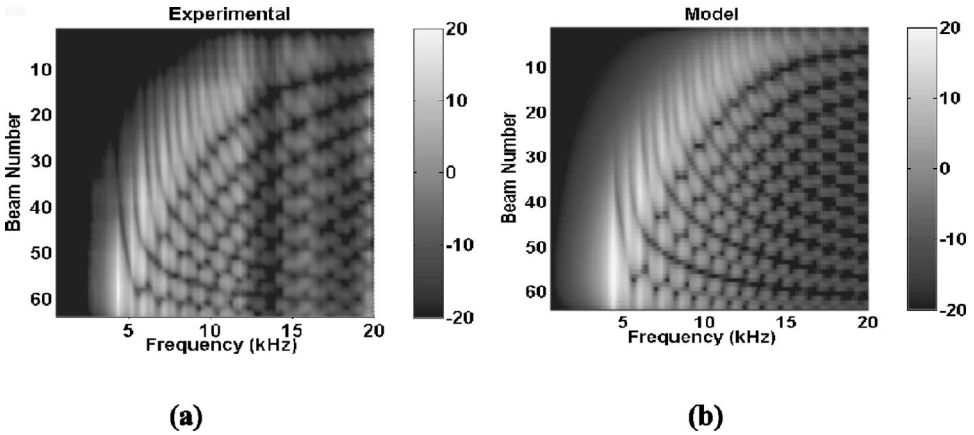

FIG. 11. A comparison of the velocity sensitivity (unit: dB *re* 1.0 mm/s/Pa) spectra of the 64-beam ABM between the measured and modeled results. (a) Spectral map of the measured result. (b) Spectral map from the modeling result. The spectra were calculated using the ABM circuit model, as shown in Figure 5(b). In the simulation, model parameters were adjusted away from their theoretical values to produce the best match to the experimental results.

C. ACochlea

The experimental results from our ACochlea, as shown in Fig. 9, demonstrate clear traveling wave features. The time domain responses in Fig. 9(a) show the steadily increasing delay from Beam #6 to #26. The delay is also demonstrated in Fig. 9(c) by the increasing phase lag from Beam #6 to #26. The time domain response in Fig. 9(a) demonstrates the widening of the period of the oscillation. Correspondingly, the magnitude response in Fig. 9(b) shows a progressively decreasing cutoff frequency, viz. from about 2.3 kHz at Beam #6, to about 2.0 kHz at Beam #16, and to about 1.8 kHz at Beam #26. This steady decrease of the roll-off frequency as a function of distance along its length demonstrates the tonotopic feature of the ACochlea.

In Fig. 9(b), the magnitude responses show high-frequency rolloffs of 67, 60, and 48 dB/octave for Beams #6, 16, and 26, respectively. The spectra also show a shallow slope in the low-frequency range. These features, a shallow slope in the low-frequency range and much steeper slope at the high-frequency end, are also features of cochlear responses.

Figure 9(b) shows a small cutoff frequency range from Beam #6 to Beam #26. Two reasons mainly account for this narrow frequency range. The first reason is the small stiffness gradient on the ABM. In our ABM, the large end is only twice as wide as the small end, compared, for example, to about six times in the human BM (Wever, 1938). This small width gradient, as well as the lack of a thickness gradient in our ABM, results in a much smaller stiffness gradient than that in the human cochlea. Additionally, the presence of the pretension on the beam, T_y, which results in a string-like behavior on beams, also results in the reduction of the stiffness gradient along the ABM, as discussed in Sec. IV B. The second reason is the coupling due to the residue from the membrane cutting. We have observed residue that bridges the cuts between beams (Chen, 2005). Simulations on the ACochlear model show that 1% of the original longitudinal tension on the membrane significantly reduces the frequency range of the ABM.

Figure 12 shows a good match between the measured and modeling results. Also, they both show ripples in the low-frequency range, which are due to reflections at the end of both the ACochlea and its model. Our ACochlear model is a vetted representation of our Acochlea.

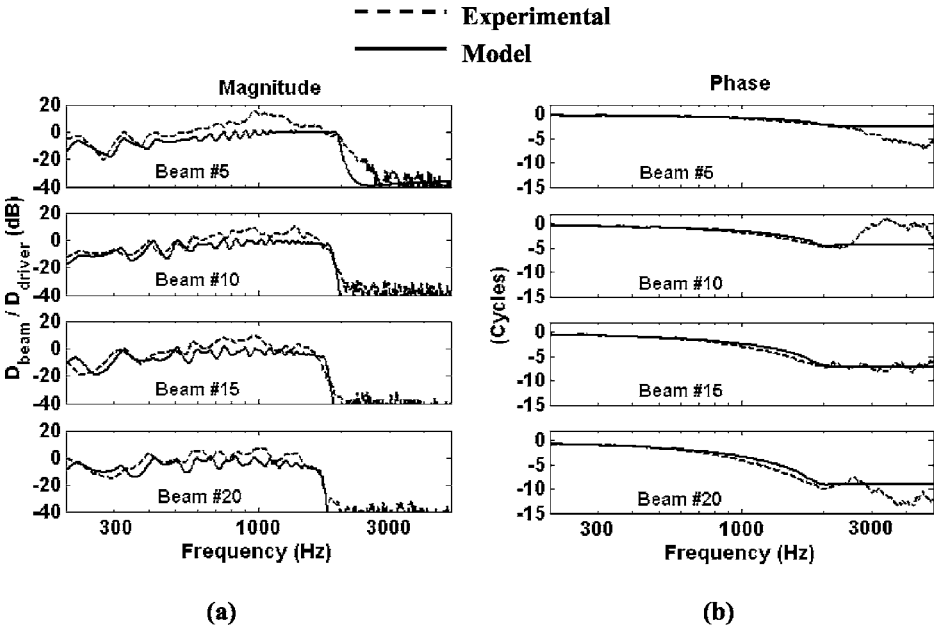

FIG. 12. A comparison of the transfer functions of the ACochlear model with the measured transfer functions from the ACochlea. The solid lines represent the modeling results and the dashed lines represent the measured results. (a) Transfer function: Magnitude in dB of the displacement ratio of the beam vibration to the driver displacement. (b) Phase response of the ratio. The phase plots of Beams #10, #15, and #20 show irregularity at frequencies above 2 kHz. This is due to the unwrapping process of the phase response. In that frequency range, the responses are near the noise level, as shown in the magnitude plots.

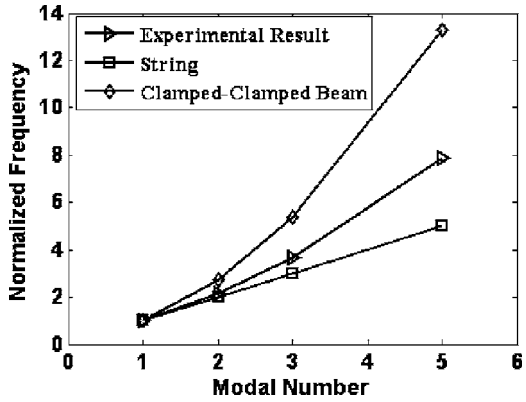

FIG. 13. A comparison of the normalized frequencies from measurements of a beam on an ABM with cuts in the membrane between beams, and those from the theoretical calculations of both a string and a pure clamped–clamped beam. Only first, second, third, and fifth modes are compared because the fourth mode is not discernible in the experimental results. The normalized frequencies from the measurements lie between two theoretical cases, which indicate that the beam vibrates neither like a string nor a pure clamped–clamped beam.

D. Piezomembrane

As shown in Fig. 10, the sensitivity of the piezofilm is about 30 mV/μm, which is not very high. This is largely because when the beam vibrates, the membrane is compressed/extended at the edge but is extended/compressed in the middle of the beam. Charges generated by these contradictory deformations partly cancel each other, reducing the piezosensitivity. A possible solution would be to attach the piezomembrane only at the edge of the beam. Lechner (Lechner, 1993) employed this design in his piezosensor.

VI. CONCLUSIONS

We have presented the construction, measurements, and the modeling of an artificial cochlea. The measurement results from this ACochlea demonstrate some cochlea-like features. The modeling results for both the ABM and the ACochlea show patterns similar to their experimental counterparts. Thus, we believe that we know how to evaluate the incorporation of various materials, rather than build a new ACochlea for every material proposed.

Future work is needed to make the ACochlea useful as a practical acoustic sensor. A large width gradient of the ABM will help increase its stiffness gradient and thus the frequency range of the ACochlea, which is likely a critical performance criterion. The tension on the membrane substrate both affects longitudinal coupling and reduces the ABM stiffness gradient. Both factors will deteriorate the frequency selectivity of our ACochlea. Materials and fabrication processes are needed to produce a membrane substrate with minimum tension. Additionally an artificial middle ear is needed to convert acoustic signals into a vibrating driver, eliminating the need for the piezostack driver, while properly matching the low impedance acoustic interface to the high impedance fluid interface of the ACochlea. A cover on the lower side of the Acochlea, creating a closed, water tight, underside channel using a cover would have virtually no effect on performance.

ACKNOWLEDGMENTS

The authors would like to thank two anonymous reviewers for their relevant comments. This work was supported by DARPA Contract No. N0001400C0314 and NIH Grant No. R01 DC00029.

[1]Note that in this paper, we limit the usage of the word "model" only to refer to the computational model. Any mechanical cochlear model will be identified as a mechanical cochlea, or an artificial cochlea, or simply ACochlea.

Chadwick, R. S., and Adler, D. (**1975**). "Experimental observations of a mechanical cochlear model," J. Acoust. Soc. Am. **58**, 706–710.

Chen, F. (2005). "A hydro-mechanical biomimetic cochlea: experiments and models" Ph.D dissertation, Boston University.

Dallos, P. (**1996**). "Overview: cochlear neurobiology," in *The Cochlea*, edited by P. Dallos, A. N. Popper, and R. R. Fay (Springer-Verlag, New York), Vol. 8, pp. 1-5.

Haronian, D., and MacDonald, N. C. (**1996**). "A micromechanics-based frequency-signature sensor," Sens. Actuators, A **53**, 288–298.

Hemmert, W., Durig, U., Despont, M., Drechsler, U., Genolet, G., Vettiger, P., and Freeman, D. M. (**2003**). "A life-sized, hydrodynamical, micromechanical inner ear," in *Biophysics of the Cochlea: From Molecules to Models*, edited by A. W. Gummer (World Scientific, Singapore), pp. 409–416.

Hubbard, A. E., and Mountain, D. C. (**1996**). "Analysis and synthesis of cochlear mechanical function using models," in *Auditory Computation*, edited by H. L. Hawkins, T. A. McMullen, A. N. Popper, and R. R. Fay (Springer-Verlag, New York), Vol. 6, pp. 62–120.

Lechner, T. P. (**1993**). "A hydromechanical model of the cochlea with nonlinear feedback using PVF2 bending transducer," Hear. Res. **66**, 202–212.

Leong, M. P., Jin, C. T., and Leong, P. H. (2003). "*An FPGA-based electronic cochlea*," EURASIP Journal on Applied Signal Processing **7**, 629–638.

Lim, K. M., Fitzgerald, A. M., Steele, C. R., and Puria, S. (**2000**). "Building a physical cochlear model on a silicon chip," in *Recent Developments in Auditory Mechanics*, edited by H. Wada, T. Takasaka, K. Ikeda, K. Ohyama, and T. Koike (World Scientific, Singapore), pp. 223–229.

Lyon, R. F., and Mead, C. (**1988**). "An analog electronic cochlea," IEEE Trans. Acoust., Speech, Signal Process. **ASSP–36**, 1119–1134.

Patuzzi, R. (**1996**). "Cochlear micromechanics and macromechanics," in *The Cochlea*, edited by P. Dallos, A. N. Popper, and R. R. Fay (Springer-verlag, New York), Vol. **8**, pp. 186–257.

Peterson, L. C., and Bogert, B. P. (**1950**). "A dynamic theory of the cochlea," J. Acoust. Soc. Am. **22**, 369–381.

Tanaka, K., Abe, M., and Ando, S. (1998). "*A novel mechanical cochlea fishbone with dual sensor/actuator characteristics*," IEEE/ASME Trans. Mechatron. **3**, 98–105.

Tonndorf, J. (**1959**). "Beats in cochlear models," J. Acoust. Soc. Am. **31**, 608–619.

von Bekesy, G. (**1960**). *Experiments in Hearing* (McGraw-Hill, New York).

Wever, E. G. (**1938**). "The width of the basilar membrane in man," Ann. Otol. Rhinol. Laryngol. **47**, 37–47.

White, R. D., and Grosh, K. (**2002**). "Design and characterization of a MEMS piezoresistive cochlear-like acoustic sensor," *IMECE'02, 2002 ASME International Mechanical Engineering Congress and Exposition*, New Orleans, LA.

White, R. D., and Grosh, K. (**2005**). "Microengineered hydromechanical cochlear model," Proc. Natl. Acad. Sci. U.S.A. **102**, 1296–1301.

Wittbrodt, M. J., Steele, C. R., and Puria, S. (**2004**). "Fluid–structure interaction in a physical model of the human cochlea," *148th Meeting of the Acoustical Society of America*, San Diego, CA.

Yang, Z. (2004). "Low-frequency analog integrated circuit design using current-mode techniques," Ph.D dissertation, Boston University.

Zhou, G., Bintz, L., Anderson, D. Z., and Bright, K. E. (**1993**). "A life-sized physical model of the human cochlea with optical holographic readout," J. Acoust. Soc. Am. **93**, 1516–1523.

Zwislocki, J. (**1950**). "Theory of the acoustical action of the cochlea," J. Acoust. Soc. Am. **22**, 778–784.